were used to measure the vertically polarized XX photons, and horizontally and vertically polarized X photons. The time between detection of XX photons and X photons was measured by a time interval analyser.

Photons can be counted over a number of hours by compensating for fluctuations in excitation and detection efficiency over time. This is achieved by determining the degree of correlation from the ratio of the two correlations measured simultaneously, each normalized by the number of pairs detected in different laser cycles.

The approach is valid for unpolarized sources, and unpolarizing transmission of the light collection system up to the wave plates. Our system satisfies these requirements, as the emission was unpolarized within error, and the transmission was only weakly polarizing. For the results of Fig. 2, a single half or quarter wave plate was inserted directly after the collection lens to select the measurement basis for the exciton and biexciton photons simultaneously, and the transmission was zero within experimental error. For the measurements of Fig. 3, a quarter wave and half wave plate was used before each spectrometer to select the polarization detection basis for the exciton and biexciton independently, and the transmission was only ~10% polarizing. The total number of coincident pairs detected over the course of an experiment is typically up to 1,000, which dictates the measurement errors.

Quantum tomography analysis. The probability that a photon pair is detected with a selected polarization combination was determined experimentally from pairs of two photon correlations measured simultaneously. 16 such measurements were used to construct each two photon density matrix, using the polarization combinations and methods of ref. 24. The density matrix fully describes the two-photon quantum state, and thus can be used to test for entanglement. The test we chose is that of the largest eigenvalue, which is a general test that makes no assumption about the nature of the entangled state, in contrast to a Bell inequality, for which violation is maximal when the entangled state corresponds to that for which the polarization measurement bases were chosen. For an unpolarized classical source, the probability that a photon pair exists in any given polarization state cannot exceed 0.5, therefore an eigenvalue >0.5 signifies the presence of entanglement.

Received 28 July; accepted 16 November 2005.

1. Walls, D. F. & Milburn, G. J. *Quantum Optics* (Springer, Berlin, 1994).
2. Bouwmeester, D., Ekert, A. K. & Zeilinger, A. *The Physics of Quantum Information* (Springer, Berlin, 2000).
3. Ekert, A. K. Quantum cryptography based on Bell's theorem. *Phys. Rev. Lett.* **67**, 661–663 (1991).
4. Gisin, N., Ribordy, G., Tittel, W. & Zbinden, H. Quantum cryptography. *Rev. Mod. Phys.* **74**, 145–195 (2002).
5. Knill, E., Laflamme, R. & Milburn, G. J. A scheme for efficient quantum computation with linear optics. *Nature* **409**, 46–52 (2001).
6. Benson, O., Santori, C., Pelton, M. & Yamamoto, Y. Regulated and entangled photons from a single quantum dot. *Phys. Rev. Lett.* **84**, 2513–2516 (2000).
7. Stevenson, R. M. *et al.* Quantum dots as a photon source for passive quantum key encoding. *Phys. Rev. B* **66**, 081302 (2002).
8. Santori, C., Fattal, D., Pelton, M., Solomon, G. S. & Yamamoto, Y. Polarization-correlated photon pairs from a single quantum dot. *Phys. Rev. B* **66**, 045308 (2002).
9. Ulrich, S. M., Strauf, S., Michler, P., Bacher, G. & Forchel, A. Triggered polarization-correlated photon pairs from a single CdSe quantum dot. *Appl. Phys. Lett.* **83**, 1848–1850 (2003).
10. Shih, Y. H. & Alley, C. O. New type of Einstein-Podolsky-Rosen-Bohm experiment using pairs of light quanta produced by optical parametric down conversion. *Phys. Rev. Lett.* **61**, 2921–2924 (1988).
11. Ou, Z. Y. & Mandel, L. Violation of Bell's inequality and classical probability in a two-photon correlation experiment. *Phys. Rev. Lett.* **61**, 50–53 (1988).
12. Kiess, T. E., Shih, Y. H., Sergienko, A. V. & Alley, C. O. Einstein-Podolsky-Rosen-Bohm experiment using pairs of light quanta produced by type-II parametric down-conversion. *Phys. Rev. Lett.* **71**, 3893–3897 (1993).
13. Fattal, D. *et al.* Entanglement formation and violation of Bell's inequality with a semiconductor single photon source. *Phys. Rev. Lett.* **92**, 037903 (2004).
14. Yuan, Z. *et al.* Electrically driven single-photon source. *Science* **295**, 102–105 (2002).
15. Edamatsu, K., Oohata, G., Shimizu, R. & Itoh, T. Generation of ultraviolet entangled photons in a semiconductor. *Nature* **431**, 167–170 (2004).
16. Santori, C., Fattal, D., Vučković, J., Solomon, G. S. & Yamamoto, Y. Indistinguishable photons from a single-photon device. *Nature* **419**, 594–597 (2002).
17. Aspect, A., Grangier, P. & Roger, G. Experimental realization of Einstein-Podolsky-Rosen-Bohm Gedankenexperiment: A new violation of Bell's inequalities. *Phys. Rev. Lett.* **49**, 91–94 (1982).
18. Gammon, D., Snow, E. S., Shanabrook, B. V., Katzer, D. S. & Park, D. Fine structure splitting in the optical spectra of single GaAs quantum dots. *Phys. Rev. Lett.* **76**, 3005–3008 (1996).
19. Bimberg, D., Grundmann, M. & Ledentsov, N. N. *Quantum Dot Heterostructures* (Wiley, Chichester, 1999).
20. Young, R. J. *et al.* Inversion of exciton level splitting in quantum dots. *Phys. Rev. B* **72**, 113305 (2005).
21. Thompson, R. M. *et al.* Single-photon emission from exciton complexes in individual quantum dots. *Phys. Rev. B* **64**, 201302 (2001).
22. Rodt, S. *et al.* Repulsive exciton-exciton interaction in quantum dots. *Phys. Rev. B* **68**, 035331 (2003).
23. White, A. G., James, D. F. V., Eberhard, P. H. & Kwiat, P. G. Nonmaximally entangled states: Production, characterization, and utilization. *Phys. Rev. Lett.* **83**, 3103–3107 (1999).
24. James, D. F. V., Kwiat, P. G., Munro, W. J. & White, A. G. Measurement of qubits. *Phys. Rev. A* **64**, 052312 (2001).
25. Kwiat, P. G., Barraza-Lopez, S., Stefanov, A. & Gisin, N. Experimental entanglement distillation and 'hidden' non-locality. *Nature* **409**, 1014–1017 (2001).
26. Santori, C., Pelton, M., Solomon, G., Dale, Y. & Yamamoto, Y. Triggered single photons from a quantum dot. *Phys. Rev. Lett.* **86**, 1502–1505 (2001).
27. Pelton, M. *et al.* Efficient source of single photons: A single quantum dot in a micropost microcavity. *Phys. Rev. Lett.* **89**, 233602 (2002).
28. Bennett, A. J., Unitt, D. C., Atkinson, P., Ritchie, D. & Shields, A. J. High performance single photon sources from photolithographically defined pillar microcavities. *Opt. Express* **13**, 50–55 (2005).
29. Bayer, M. & Forchel, A. Temperature dependence of the exciton homogeneous linewidth in $In_{0.60}Ga_{0.40}As/GaAs$ self-assembled quantum dots. *Phys. Rev. B* **65**, 041308 (2002).
30. Stevenson, R. M. *et al.* Magnetic-field-induced reduction of the exciton polarization splitting in InAs quantum dots. *Phys. Rev. B* (in the press).

Acknowledgements We acknowledge continued support from M. Pepper. This work was partially funded by the EU projects RAMBOQ, QAP and SANDiE, and by the EPSRC through the IRC for Quantum Information Processing.

Author Information Reprints and permissions information is available at npg.nature.com/reprintsandpermissions. The authors declare no competing financial interests. Correspondence and requests for materials should be addressed to R.M.S. (mark.stevenson@crl.toshiba.co.uk).

LETTERS

Ultrafast superheating and melting of bulk ice

H. Iglev[1], M. Schmeisser[1], K. Simeonidis[1], A. Thaller[1] & A. Laubereau[1]

The superheating of a solid to a temperature beyond its melting point, without the solid actually melting, is a well-known phenomenon. It occurs with many substances[1–3], particularly those that can readily be produced as high-quality crystals. In principle, ice should also be amenable to superheating. But the complex three-dimensional network of hydrogen bonds that holds water molecules together and gives rise to unusual solid and liquid properties[4–11] strongly affects the melting behaviour of ice[12–14]; in particular, ice usually contains many defects owing to the directionality of its hydrogen bonds. However, simulations are readily able to 'create' defect-free ice that can be superheated[15,16]. Here we show that by exciting the OH stretching mode of water, it is possible to superheat ice. When using an ice sample at an initial temperature of 270 K, we observe an average temperature rise of 20 ± 2 K that persists over the monitored time interval of 250 ps without melting.

We have performed ultrafast temperature jump measurements in ice (for details on the experimental set-up and the sample preparation, see the Methods section) using the OH- and OD-stretching vibrations for rapid heating of the sample[17,18]. The same vibrational modes are known to be sensitive probes for H-bonding[19,20] and represent suitable spectral tools to distinguish local ice or water structures with a time resolution of a few picoseconds[20,21]. To illustrate this point, the steady-state infrared absorption spectrum of HDO:D_2O is shown in Fig. 1a for various temperature values. In the range 2,000–4,000 cm^{-1} the well-known OD- and OH-bands (left and right) occur with significant changes of position (blueshift) and shape with temperature. Figure 1b presents the same data as thermal differential spectra for $\Delta T = 20$ K. The spectrum corresponding to melting of the ice sample reduced by a factor of five is also shown in the Fig. 1b. The potential of the molecular vibrations as local probes of temperature and melting is readily seen.

Examples for the time-resolved differential spectra measured in a 2.5-μm-thick HDO:D_2O (15 M) ice specimen at 200 K are presented in Fig. 2. It shows ultrafast heating by two different processes via infrared absorption of the OH- or the OD-stretching vibration. The transient spectra taken 50 ps after excitation are shown in Fig. 2a. The absorption changes are plotted for pump pulses of 3.0 μJ at 3,290 cm^{-1} (OH-pumping, blue points) and 2.7 μJ at 2,435 cm^{-1} (OD-pumping, red points). The adjustment of the pump-pulse energies ensures that approximately equal amounts of energy are deposited in the sample for both frequency settings. Both excitation schemes induce almost the same spectral changes in the HDO ice, indicating that the OH- and OD-oscillators are already at $t_D = 50$ ps in a local equilibrium. The similarity of the time-resolved data in Fig. 2a and the thermal differential spectra presented in Fig. 1b confirms induced heating of the sample. A comparison of the experimental data against differential spectra computed for various isochoric temperature jumps and the associated simultaneous pressure increase suggests an average temperature rise of 20 ± 2 K in the ice sample (Fig. 2b, see also the Methods section for further details). The isochoric pressure increase is estimated to be ~26 MPa.

The time evolution of the spectral changes induced by OH-pumping is depicted as a contour plot in Fig. 2c, showing that the frequency shift of the hydroxilic stretching modes—which appears as induced absorption in the high-frequency wings, indicated in red—has terminated after 20 ps. The temporal evolution of the spectral shift for both OH- and OD-pumping is documented by more quantitative data in Fig. 2d and e, for fixed probing frequencies of 2,435 cm^{-1} (OD probing, Fig. 2d) and 3,280 cm^{-1} (OH probing, Fig. 2e). At short delay times, fast signal changes occur at rates comparable to our time resolution under both excitation conditions, at both probing frequencies. (The signal overshoot for OH-pumping, shown by blue points in Fig. 2e at around $t_D = 0$ ps possibly involves a coherent pump-probe artefact in addition to depletion of the vibrational ground state.) For delay times longer than 20 ps, amplitude levels are constant. We can fit the data using a simple relaxation model with two assumed exponential time constants, and obtain a short relaxation time of $\tau_1 \leq 0.5$ ps consistent with the reported OH-lifetime of HDO ice[17,18] and a longer relaxation time of

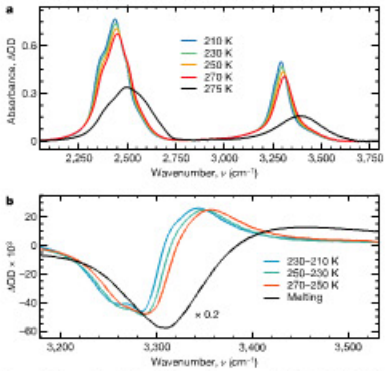

Figure 1 | Conventional infrared absorption spectra of HDO:D_2O (15 M). **a**, Absorption spectra of hexagonal ice in the OH- and OD-stretching region at various temperatures from 210 K (blue) to 270 K (red). The spectrum of the molten sample at 275 K (black line) is also shown. **b**, Same data as in **a** plotted as thermal differential spectra with $\Delta T = 20$ K. For a better view, the spectrum corresponding to melting of the ice sample is scaled by a factor of 0.2 (275–270 K, black line).

[1]Physik-Department, Technische Universität München, James-Franck-Strasse, D-85748 Garching, Germany.

$\tau_1 = 8.7 \pm 0.5$ ps attributed to the thermalization of the hydrogen bonding network of the ice specimen, that is, energy redistribution among low-frequency intermolecular vibrations. The process involves an average temperature rise of 20 ± 2 K that persists beyond 250 ps.

Figure 3 presents data similar to those shown in Fig. 2, except that the ice sample has an initial temperature of 270 K and that the pump frequencies are tuned to match the temperature-shifted band maxima (3,310 cm^{-1}, blue points; 2,450 cm^{-1}, red points). The time-resolved differential spectra for $t_D = 50$ ps in Fig. 3a show a striking similarity to the spectra in Fig. 2a, exhibiting a blueshift of the hydrocilic bands but no evidence for melting. Similarly, the time evolution of the probe signals (Fig. 3c–e) only suggests an increase in the temperature of the sample that does not cause melting. The energy transfer between OH- and OD-modes occurs slightly faster than at 200 K, with the new thermal equilibrium established within 15 ps. The behaviour is reflected by a shorter thermal relaxation time obtained with the two-stage relaxation model, $\tau_1 = 5.4 \pm 0.5$ ps (Fig. 3d and e; we can again place only an upper limit on the fast relaxation time, $\tau_1 \leq 0.5$ ps).

The similar behaviour observed at the two temperatures suggests that the optical excitation induces the same process in both ice samples: heating of the ice, rather than melting. To verify this point, we numerically generate a hypothetical thermal differential spectrum for HDO:D_2O ice at a temperature that is above the ice melting point of 274.8 K. For this, we extrapolate the dependence of the spectral position of the $\Delta T = 20$ K thermal difference spectrum on initial sample temperature, noting that both amplitude and spectral shape depend only slightly on initial temperature (Fig. 1b). The results of the simulation for different temperature jumps (which account for the effects of isochoric pressure increases) are compared with the measured spectrum in Fig. 3b, indicating that optical excitation has heated the 270 K ice sample to an averaged bulk temperature of 290 ± 2 K.

According to simulations, the stability of the superheated state of metals is limited by defect concentrations of the order of several per cent[22], whereas experimental studies observed melting already at a vacancy concentration one order of magnitude smaller[13]. We estimate the chemical impurities of our sample to be of the order of 10^{-4}, representing a lower limit to the defect concentration. The strength of hydrogen bonds is notably smaller than that of covalent and metallic bonds, resulting in higher fluctuations of the hydrogen-bonded network in ice and thus enhanced formation and migration of structural defects[24]; in the case of large topological defects with a lifetime of 0.5 ns, these are predicted to induce bulk melting close to the common melting temperature[25]. In general, defect-free crystals can readily be superheated[13,26]; but once a critical defect concentration is present, it will induce melting and thus interfere with superheating[25]. We note that evidence for the melting of our samples within 250 ps after energy deposition is lacking. The topological defects considered in ref. 25 clearly do not play a significant role on this timescale.

When using larger temperature jumps, we do observe melting. Figure 4 shows time-resolved data for OH-pumping at 3,275 cm^{-1}, obtained with a 1-μm-thick sample of HDO:H_2O (15 M) ice with an initial temperature of 265 K. The absorption changes at four spectral positions in the OH-stretching region measured at $t_D = 50$ ps are plotted versus density of deposited energy (Fig. 4a). As long as the deposited energy density does not exceed 55 ± 5 J cm^{-3}, the spectral amplitudes are proportional to the excitation level (and average temperature rise), as is expected for laser-induced heating. Similar to the data of Fig. 3 for the HDO:D_2O sample, the superheated ice state of HDO:H_2O is found to persist over the monitored time interval of 250 ps (data not shown).

When the deposited energy density exceeds 55 J cm^{-3}, all excitation curves exhibit a change in their slope (see Fig. 4a) that is accompanied by a significant broadening of the transient absorption spectra. The difference of two transient spectra measured above 55 J cm^{-3} agrees well with the thermal differential spectrum corresponding to the ice–liquid phase transition (data not shown), suggesting that the sample undergoes partial melting. The data in Fig. 4a suggest an average temperature value of 292 ± 5 K as the limit for superheating of this ice sample, a value in fair agreement with recent calculations by Luo *et al.*[15].

Data on the time evolution of the melting process in the HDO:H_2O sample after excitation with 95 ± 5 J cm^{-3} are presented in Fig. 4b. For short delay times, absorption first decreases rapidly (see inset of Fig. 4b) and then more slowly on the timescale of several picoseconds (τ_2). In contrast to the dynamics observed for superheating (below 55 J cm^{-3}), where the signal curve reaches a constant amplitude within 15 ps, the data in Fig. 4b display an additional relaxation mode extending over 150 ps that appears to be connected to partial melting of the ice specimen. Incorporating a third exponential time constant in the relaxation model yields $\tau_3 = 45 \pm 5$ ps for the slowest process (see solid curves in Fig. 4b). The exact character of this time constant is not well understood at the present time. Compared to the lifetime of hydroxilic vibrations (below 1 ps) and the measured thermalization time of ice of several picoseconds, this novel relaxation feature persists over a notably longer time period; this is expected for a collective process such as melting, which involves many molecules. Deeper understanding of this intriguing feature will need to await more detailed studies of the mechanisms underlying the solid–liquid phase transition.

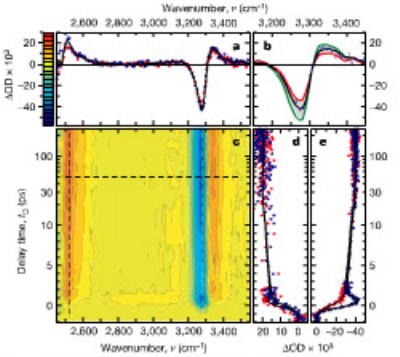

Figure 2 | Ultrafast heating of HDO:D_2O ice from 200 K to 220 K. Subpicosecond excitation at 3,290 cm^{-1} (OH-pumping, blue points) and 2,435 cm^{-1} (OD-pumping, red points). Error bars are s.d. **a**, Transient differential absorption spectra ($\Delta OD \times 10^3$) taken 50 ps after excitation. The solid black line indicates the differential absorption spectrum calculated for a temperature increase of 20 K. **b**, Magnification of the OH-range from panel a, with calculated isochoric thermal differential spectra for $\Delta T = 15$ K (red), 20 K (black) and 25 K (green). **c**, Contour plot of the spectral changes induced by OH-pumping as a function of probe frequency and delay time. Induced absorption is indicated by red and bleaching by blue, with contour values given in the colour scale next to **a**. We note that the delay time is on a linear scale to 10 ps, and on a logarithmic scale for longer delays. **d**, **e**, Induced absorption ($\Delta OD \times 10^3$) at 2,520 cm^{-1} (**d**) and bleaching (negative $\Delta OD \times 10^3$) at 3,280 cm^{-1} (**e**) versus delay time. Solid lines are fits using a simple relaxation model with two assumed exponential time constants.

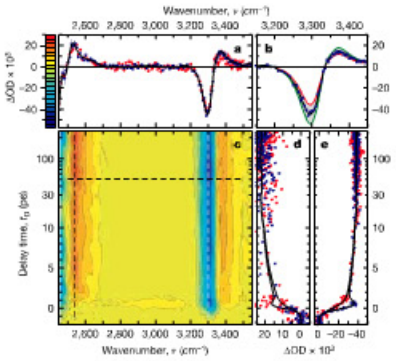

Figure 3 | Superheating of HDO:D_2O ice from 270 K to 290 K. Excitation at 3,310 cm^{-1} (blue points) and 2,450 cm^{-1} (red points). Error bars are s.d. **a**, Transient differential absorption spectra measured 50 ps after ultrafast heating. The black solid curve represents an extrapolated thermal differential absorption spectrum for a transient ice state at 290 K and pressure of 26 MPa. **b**, Magnification of the OH-range with extrapolated isochoric thermal differential absorption spectra for $\Delta T = 15$ K (red), 20 K (black) and 25 K (green). **c**, Contour plot of the spectral changes induced by OH-pumping, as a function of probe frequency and delay time. **d**, **e**, Induced absorption at 2,535 cm^{-1} (**d**) and bleaching at 3,300 cm^{-1} (**e**) versus delay time.

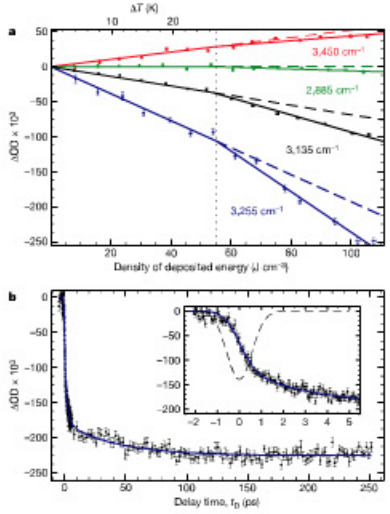

Figure 4 | Superheating and (partial) melting of ice. Time-resolved absorption changes ($\Delta OD \times 10^3$) measured in HDO:H_2O (15 M) ice at 265 K after OH-pumping at 3,275 cm^{-1} (experimental points, error bars are s.d.). **a**, Absorption changes taken at $t_D = 50$ ps and various spectral positions versus average density of deposited energy in the probed volume; lines are guides to the eye. The upper abscissa scale denotes the average temperature jump ΔT. **b**, Temporal evolution of the induced bleaching in the OH-band at 3,255 cm^{-1}; the solid curve indicates the predictions of the extended relaxation model. The inset shows the short time dynamics ($\Delta OD \times 10^3$ versus t_D) together with the shape of the pump pulse (dashed line).

METHODS

Subpicosecond infrared spectrometer. Our experimental system was described recently[26] and is just briefly mentioned here. The infrared pulses are delivered by laser-pumped parametric oscillator-amplifier devices with durations of 0.7 ps (0.9 ps), spectral widths of 24 cm^{-1} (19 cm^{-1}) and typical energies of 10 μJ (3.0 μJ). Computer-controlled tuning is provided in the range 1,700–3,700 cm^{-1} (2,300 to 3,700 cm^{-1}). Numbers in brackets refer to the pump pulses. The pump beam diameter in the sample of approximately 150 μm is a factor of two larger than that of the probe, so that only the central part of the interaction volume with maximum excitation is monitored. The energy transmittances $T(\nu)_\parallel$, $T(\nu)_\perp$ of the probing pulse through the excited sample are measured for parallel (∥) and perpendicular (⊥) polarizations with respect to the linear polarization of the pump beam and compared with the probe transmittance $T(\nu)_0$ for blocked excitation. In this way the induced changes of optical density $\Delta OD_{\parallel,\perp}$ are determined for various probe frequencies ν and delay times t_D. The isotropic absorption signal, defined as $\Delta OD(\nu, t_D)_{iso} = -[\log(T/T_0)_\parallel + 2\log(T/T_0)_\perp]/3$ is determined and plotted as $\Delta OD \times 10^3$ in Figs 2–4, that is, independently of a possibly induced optical anisotropy.

Preparation of the investigated ice crystals. The samples are produced by slowly cooling a mixture of HDO (where D is deuterated H) in D_2O or in H_2O (15 M) between two CaF_2 windows with a suitable spacer (2.5 or 1.0 μm) in a cryostat to 180 K and adjusting the desired temperature later on. The isotopic mixtures are prepared from appropriate amounts of tri-distilled H_2O and D_2O (>99.9 at.%D) without further purification. The melting points are measured to be 274.8 ± 0.3 K and 273.4 ± 0.3 K for HDO:D_2O and HDO:H_2O, respectively.

Isochoric temperature jump. To calibrate our 'picosecond thermometer' we performed careful steady-state measurements of the (isobaric) temperature change of the absorption spectrum using Fourier transform infrared (FTIR) spectroscopy and also our subpicosecond infrared spectrometer (with the pump pulse blocked). In addition we took into account that the ultrafast temperature rise of the sample occurs at constant volume leading to a simultaneous pressure increase, because thermal volume expansion is relatively slow on a nanosecond timescale only. The simultaneous pressure change in the crystal during a fast temperature rise at constant volume is incorporated by using the reported isothermal pressure shift of the vibrational band and thermodynamic parameters of ice. The isobaric temperature coefficients of the OH-band position of HDO:D_2O are measured to be $(\Delta\nu_{OH}/\Delta T)_p = 0.28 \pm 0.01$ cm^{-1} K^{-1} at 200 K and 0.41 ± 0.01 cm^{-1} K^{-1} at 270 K. The required thermodynamic parameters are the coefficient of thermal volume expansion, 155 MK^{-1}, and the isothermal compressibility of 0.12 GPa^{-1} (refs 27 and 28), from which the isochoric pressure increase of 1.3 MPa K^{-1} is derived. Using the isothermal pressure downshift[9,10] of -78 ± 7 cm^{-1} GPa^{-1} for the OH band of ice I_h (ref. 29) we estimate the isochoric shifts to be $(\Delta\nu_{OH}/\Delta T)_V = 0.18 \pm 0.02$ cm^{-1} K^{-1} at 200 K and 0.31 ± 0.02 cm^{-1} K^{-1} at 270 K, respectively. The OD-stretching mode is expected to display a corresponding shift approximately a factor of $\sqrt{2}$ smaller. The computed results for the thermal differential spectra for isochoric temperature jumps of 15 K (green line), 20 K (black) and 25 K (cyan) are shown in Fig. 2b. From comparison with additional curves we deduce an accuracy of our picosecond thermometer of ±2 K in this sample.

We have verified experimentally that the temperature dependence of the broader OH-stretching band of H_2O can be applied in an analogous manner for a picosecond thermometer. The measuring accuracy in the HDO:H_2O (15 M) ice sample is somewhat reduced to ±3 K.

Received 11 May; accepted 3 November 2005.

1. Luo, S. N. *et al.* Maximum superheating and undercooling: systematics, molecular dynamics simulations, and dynamic experiments. *Phys. Rev. B* 68, 134206 (2003).

2. Luo, S. N. & Ahrens, T. J. Shock-induced superheating and melting curves of geophysically important minerals. *Phys. Earth Planet. Inter.* **143–144**, 369–386 (2004).
3. Huang, K. C., Wang, T. & Ioannopoulos, J. D. Superheating and induced melting at semiconductor interface. *Phys. Rev. Lett.* **94**, 175702 (2005).
4. Jin, Z. H., Gumbsch, P., Lu, K. & Ma, E. Melting mechanisms at the limit of superheating. *Phys. Rev. Lett.* **87**, 055703 (2001).
5. Cahn, R. W. Melting and the surface. *Nature* **323**, 668–669 (1986).
6. Mishima, O. & Stanley, H. E. The relationship between liquid, supercooled and glassy water. *Nature* **396**, 329–335 (1998).
7. Wernet, Ph. *et al.* The structure of the first coordination shell in liquid water. *Science* **304**, 995–999 (2004).
8. Tonne, R., Bartolini, P. & Righini, R. Structural relaxation in supercooled water by time-resolved spectroscopy. *Nature* **428**, 296–298 (2004).
9. Ludwig, R. Water: from clusters to the bulk. *Angew. Chem. Int. Edn Engl.* **40**, 1808–1827 (2001).
10. Tse, J. S. *et al.* The mechanisms for pressure-induced amorphization of ice I$_h$. *Nature* **400**, 647–649 (1999).
11. Tulk, C. A. *et al.* Structural studies of several distinct metastable forms of amorphous ice. *Science* **297**, 1320–1323 (2002).
12. Mishima, O., Calvert, L. D. & Whalley, E. 'Melting ice' I at 77 K and 10 kbar: a new method of making amorphous solids. *Nature* **310**, 393–395 (1984).
13. Engemann, S. *et al.* Interfacial melting of ice in contact with SiO$_2$. *Phys. Rev. Lett.* **92**, 205701 (2004).
14. Ruan, Ch.-Y., Lobastov, V. A., Vigliotti, F., Chen, S. & Zewail, A. H. Ultrafast electron crystallography of interfacial water. *Science* **304**, 80–84 (2004).
15. Luo, S. N., Strachan, A. & Swift, D. C. Deducing solid-liquid interfacial energy from superheating or supercooling: application to H$_2$O at high pressures. *Model. Simul. Mater. Sci. Eng.* **13**, 321–328 (2005).
16. McBride, C., Vega, C., Sanz, E., MacDowell, L. G. & Abascal, J. L. F. The range of metastability of ice-water melting for two simple models of water. *Mol. Phys.* **103**, 1–5 (2005).
17. Laenen, R., Simeonidis, K. & Laubereau, A. Generation of sub-ps IR pulses via parametric processes and application to transient spectroscopy of molecules. *Laser Phys.* **9**, 234–238 (1999).
18. Woutersen, S., Emmerichs, U., Nienhuys, H. K. & Bakker, H. J. Anomalous temperature dependence of vibrational lifetimes in water and ice. *Phys. Rev. Lett.* **81**, 1106–1109 (1998).
19. Graener, H., Seifert, G. & Laubereau, A. New spectroscopy of water using tunable picosecond pulses in the infrared. *Phys. Rev. Lett.* **66**, 2092–2095 (1991).
20. Laenen, R., Rauscher, C. & Laubereau, A. Dynamics of local substructures in water observed by ultrafast infrared hole burning. *Phys. Rev. Lett.* **80**, 2622–2625 (1998).
21. Woutersen, S., Emmerichs, U. & Bakker, H. J. Femtosecond Mid-IR pump-probe spectroscopy of liquid water: evidence for a two-component structure. *Science* **278**, 658–660 (1997).
22. Fecht, H. J. Defect-induced melting and solid-state amorphization. *Nature* **356**, 133–135 (1992).
23. Göreckí, T. Comments on vacancies and melting. *Scr. Metall.* **11**, 1051–1053 (1977).
24. Girshins, N. & Buch, V. Structure and dynamics of orientational defects on ice I. *J. Chem. Phys.* **120**, 5217–5225 (2004).
25. Donadio, D., Raiteri, P. & Parrinello, M. Topological defects and bulk melting of hexagonal ice. *J. Phys. Chem. B* **109**, 5421–5424 (2005).
26. Laenen, R., Simeonidis, K. & Laubereau, A. Subpicosecond spectroscopy of liquid water in the infrared: effect of deuteration on the structural and vibrational dynamics. *J. Phys. Chem. B* **106**, 408–417 (2002).
27. LaPlaca, S. & Post, B. Thermal expansion of ice. *Acta Crystallogr.* **13**, 503–505 (1960).
28. Grow, A. J. & Williamson, T. C. Linear compressibility of ice. *J. Geophys. Res.* **77**, 6348–6352 (1972).
29. Minceva-Sukarova, B., Sherman, W. F. & Wilkinson, G. R. The Raman spectra of ice (I$_h$, II, III, V, VI and IX) as functions of pressure and temperature. *J. Phys. C* **17**, 5833–5850 (1984).
30. Sivakumar, T. C., Chew, H. A. M. & Jahani, G. P. Effect of pressure on the Raman spectrum of ice. *Nature* **275**, 524–525 (1978).

Author Information Reprints and permissions information is available at npg.nature.com/reprintsandpermissions. The authors declare no competing financial interests. Correspondence and requests for materials should be addressed to H.I. (higlev@iph.tum.de).

LETTERS

Methane emissions from terrestrial plants under aerobic conditions

Frank Keppler[1], John T. G. Hamilton[2], Marc Braß[1,3] & Thomas Röckmann[1,3]

Methane is an important greenhouse gas and its atmospheric concentration has almost tripled since pre-industrial times[1,2]. It plays a central role in atmospheric oxidation chemistry and affects stratospheric ozone and water vapour levels. Most of the methane from natural sources in Earth's atmosphere is thought to originate from biological processes in anoxic environments[2]. Here we demonstrate using stable carbon isotopes that methane is readily formed *in situ* in terrestrial plants under oxic conditions by a hitherto unrecognized process. Significant methane emissions from both intact plants and detached leaves were observed during incubation experiments in the laboratory and in the field. If our measurements are typical for short-lived biomass and scaled on a global basis, we estimate a methane source strength of 62–236 Tg yr^{-1} for living plants and 1–7 Tg yr^{-1} for plant litter (1 Tg = 10^{12} g). We suggest that this newly identified source may have important implications for the global methane budget and may call for a reconsideration of the role of natural methane sources in past climate change.

Methane (CH_4) is the most abundant organic trace gas in the atmosphere (mixing ratio ~1.8 p.p.m.) and is important to both tropospheric and stratospheric chemistry. Therefore, the atmospheric CH_4 budget has been intensively studied over the past two decades using flux measurements on sources[3], global observation networks[4] and global atmospheric models[5,6]. In addition, stable carbon isotope ratios ($^{13}C/^{12}C$) have been applied to investigate sources and sinks of atmospheric CH_4 (refs 7, 8). Although uncertainties in the estimates of individual source strengths are large (50–100 Tg), it is generally thought that all major sources, including wetlands, animals, rice cultivation, biomass burning and fossil fuel production, have been identified and sum up to a global source strength of ~600 Tg yr^{-1} (refs 1, 2). However, significantly elevated CH_4 mixing ratios were recently observed in tropical regions above evergreen forests[9] indicating an additional tropical source of 30–40 Tg over the time period of the investigation (August–November), which could not be explained within the currently accepted global budget of CH_4.

Following our observations of non-enzymic production of methyl halides from senescent plants and leaf litter[10,11], we investigated the possibility of methane formation by plant material. A large set of laboratory experiments using freshly collected and dried plant material—including tree and grass leaves from C_3 and C_4 plant categories—were conducted, in which CH_4 release rates and stable carbon isotope composition ($\delta^{13}C$ values) of emissions were measured under controlled conditions (see Methods). Whereas CH_4 emissions were difficult to quantify for samples incubated in ambient air owing to the high atmospheric background levels of CH_4, production was clearly evident when samples were incubated in CH_4-free air. Emission rates typically ranged from 0.2 to 3 ng per g (dry weight) h^{-1} at 30 °C (see Supplementary Table S1). Release of CH_4 was very temperature sensitive—concentrations approximately doubled with every 10 °C increase over the range 30–70 °C (Fig. 1a), suggesting a non-enzymic rather than an enzyme-mediated process. $\delta^{13}C$ of the emitted CH_4 ranged from −51.8‰ to −68.4‰ (mean = −58.2‰, $n = 61$) and −46.9‰ to −53.1 (mean = −49.5‰, $n = 13$) for C_3 and C_4 plants, respectively. The mean value determined for C_3 plant emissions is comparable with the average $\delta^{13}C$ value for CH_4 emitted from wetlands and rice paddies (approximately −60‰; ref. 8) and thus would be generally regarded as an indication for biological production by anaerobic bacteria. Even though this possibility was remote since most of our experiments were performed under aerobic conditions, we measured CH_4 production by leaf tissue sterilized with γ-radiation (Fig. 1b, c). No significant difference, either in emission rates or $\delta^{13}C$ values of the emissions, was noted between sterilized and non-sterilized samples, thus further excluding microbial activity as the CH_4 source and clearly indicating the existence of a hitherto unknown pathway for CH_4 production in leaf tissue.

Having established CH_4 production by detached leaf tissue, we investigated the possibility of CH_4 formation by intact plants, using incubation chambers in the laboratory and in the field (see Methods). CH_4 formation was observed for all plant species investigated, with release rates ranging from 12 to 370 ng per g (dry weight) h^{-1}, thus one to two orders of magnitude higher than the emissions from detached leaf material. Furthermore, emission rates were found to increase dramatically, by a factor of 3–5 (up to 870 ng per g (dry weight) h^{-1}), when chambers were exposed to natural sunlight, an effect also observed with detached leaf tissue (see Supplementary Information). As can be seen from Fig. 2, CH_4 concentrations increased continuously when plants were incubated in chambers at ambient temperatures. We conducted most laboratory chamber experiments in a CH_4-free air atmosphere where, in addition to concentration measurements, reliable $\delta^{13}C$ measurements were also recorded when CH_4 concentrations in the chamber were above 40 p.p.b. (Fig. 2b–d). $\delta^{13}C$ values were in the range of −48‰ to −59.5‰ (mean = −52‰, $n = 29$) and −45 to −47‰ (mean = −46.5‰, $n = 11$) for C_3 and C_4 plants, respectively. Our experiments were performed in a well circulated atmosphere containing ~20% oxygen, so it was unlikely that the observed CH_4 production could have been mediated by anaerobic acetate fermentation or CO_2 reduction, since obligate anaerobes metabolize only under anoxic conditions at redox levels $E_h < -200$ mV.

Nevertheless, we conducted a series of experiments that have enabled us to unequivocally demonstrate *in situ* formation of CH_4 in plants. First, we could not detect any differences in either the emission rates or the $\delta^{13}C$ values for CH_4 produced by plants of the same species that were grown hydroponically or on soil. Second, since

[1]Max-Planck-Institut für Kernphysik, Saupfercheckweg 1, 69117 Heidelberg, Germany. [2]Department of Agriculture and Rural Development for Northern Ireland, Agriculture, Food and Environmental Science Division, Newforge Lane, Belfast BT9 5PX, UK. [3]Institute for Marine and Atmospheric Research Utrecht, Utrecht University, Princetonplein 5, 3508 TA, Utrecht, The Netherlands.